

Optical Coherence Elastography Measures Mechanical Tension in the Lens and Capsule *in situ*

XU FENG^{1,4,†}, GUO-YANG LI^{1,3,†}, YUXUAN JIANG^{1,†}, OWEN SHORTT-NGUYEN¹, AND SEOK-HYUN YUN^{1,2,*}

¹Harvard Medical School and Wellman Center for Photomedicine, Massachusetts General Hospital, 50 Blossom St., Boston, MA 02114, USA

²Harvard-MIT Division of Health Sciences and Technology, Cambridge, MA 02139, USA

³Currently with the Department of Mechanics and Engineering Science, College of Engineering, Peking University, Beijing 100871, China

⁴Currently with the Department of Bioengineering, University of Texas at Dallas, TX 75080, USA

[†]Equal contribution

*syun@hms.harvard.edu

Abstract: Lens tension is essential for accommodative vision but remains challenging to measure with precision. Here, we present an optical coherence elastography (OCE) technique that quantifies both the tension and elastic modulus of lens tissue and capsule. This method derives mechanical parameters from surface wave dispersion across a critical frequency range of 1-30 kHz. Using isolated lenses from six-month-old pigs, we measured intrinsic anterior capsular tensions of 0-20 kPa and posterior capsular tensions of 40-50 kPa, induced by intra-lenticular pressure at the cortical surface. Young's modulus (E) was 1.9 MPa for anterior capsules and 1.2 MPa for posterior capsules. Tensions in cortical tissue ($E \sim 10$ kPa) were below 1 kPa. Biaxial zonular stretching ($\sim 4\%$ strain) increased anterior capsular tension from near zero to 64 kPa. This acousto-optical method holds significant promise for diagnosing and managing accommodative dysfunctions through lens mechanics assessment in clinical settings.

1. INTRODUCTION

The crystalline lens plays a critical role in human vision by enabling fine-tuning of focus through the process of accommodation. The gradient lenticular-shape structure, consisting of the nucleus, cortex and capsule, contributes approximately 30-35% of the eye's total refractive power. Focal adjustment is achieved by changes in lens shape, driven by tension from the surrounding zonular fibers attached to the capsule at the equator of the lens. These fibers are connected to the ciliary muscle, which receive neuronal signals from the visual cortex, forming a negative-feedback loop for focusing. Although some debate persist [1-3] regarding the precise mechanical interplay between the ciliary muscle, suspensory zonular fibers, and lens capsule, the Helmholtz accommodation theory, proposed in 1856, is widely accepted [4]. According to this theory, contraction of the ciliary muscle loosens the zonular fibers, releasing tension on the lens capsule. The relaxed lens adopts a more spherical and thicker shape, shortening its short focal length for near vision. Conversely, when viewing distant objects, the ciliary muscle relaxes, allowing the zonular fibers to stretch the lens. This tension flattens the lens [5, 6], increasing its focal length for far vision.

It is well established that the accommodative tuning range of focal length declines steadily with age. A significant loss of accommodative ability, known as presbyopia, typically occurs around the age of 45, with accommodation being completely lost by the age of 65 [7, 8]. Presbyopia is primarily attributed to age-related stiffening and thickening of crystalline lens tissues [9, 10]. As the lens hardens, it becomes non-deformable, even under normal ciliary and capsular tension. In addition to lens hardening, aging-related changes in ciliary muscle function have been proposed as a potential contributor to presbyopia [11, 12]. However, several studies have demonstrated that ciliary muscles remain functional in older individuals, even after the complete loss of accommodation power [13]. The role of zonular and capsular tension in presbyopia remains poorly understood. This incomplete understanding is likely due to the challenges of evaluating ciliary muscle function *in vivo* and accurately quantifying the tension applied to the lens tissue.

The mechanical properties of lens tissues and their role in lens deformability have been extensively studied using various mechanical methods [14]. They include spinning tests [15-17], indentation [18-20], compression [21], bubble acoustics [22, 23], and atomic force microscopy [24, 25], Brillouin microscopy [26, 27], optical coherence elastography (OCE) [28-30] and ultrasound elastography [31]. Additionally, the mechanical properties of the lens capsule have been a focus of research, particularly in the context of cataract surgery. Investigations have employed methods such as inflation testing [32], stretching [33], stress-strain analysis [10, 34-36], nanoindentation [37] and atomic force microscopy [25, 38].

In this study, we present an acousto-optical method for *in situ* measurement of capsular tension with high sensitivity (on the kPa scale). Leveraging a state-of-the-art wideband OCE system [39, 40], this approach enables the precise measurement of elastic wave velocities along the lens surface over a critical frequency range (1-30 kHz) encompassing the onset of leaky surface waves. By applying an advanced elastoacoustic modeling framework, we extracted key mechanical parameters, including capsular tension, and intra-lenticular pressure (ILP), and the elastic moduli of the capsule and underlying tissues. This method was further used to quantify capsular tension under lens stretching forces. Finally, the potential clinical applications of this technique are discussed.

2. MATERIALS AND METHODS

A. Porcine sample preparation and measurement procedures

Lenses were surgically extracted from six fresh porcine eyeballs (Research 87, Inc., Boylston, MA). OCE measurements were first conducted on both the anterior and posterior sides of five intact lenses. Subsequently, capsular tension was released by cutting the capsules around the

equator dissecting micro scissors. OCE measurements were then repeated on both the anterior and posterior sides of the five relaxed lenses. For three of these lenses, the capsules were peeled off using precision tweezers, and OCE measurements were performed on the isolated lens capsules placed loosely on a holder without external tension. A home-built biaxial stretcher was used to stretch the lenses and zonules *in situ* in fresh porcine eye globes. To prepare the samples, the equator of the eye globe was cut to remove the posterior portion, and the cornea was excised to expose the lens. The sclera was sectioned into four parts, and hooks were placed on these sections for biaxial stretching. To estimate lens stretch, a 3 mm x 3 mm square ink mark was placed on the lens surface, and its deformation was recorded using a camera and analyzed with ImageJ software. All measurements were completed within 12 hours post-mortem to ensure sample integrity.

B. Optical coherence elastography (OCE)

A custom-built optical coherence tomography (OCT) system equipped with a swept laser source centered at 1300 nm was used [40, 41]. The system operated at an A-line rate of 43.2 kHz, with an optical power of less than 10 mW delivered to the sample. Mechanical stimulations were applied using a custom contact probe [41] consisting of a piezoelectric transducer (PZT) and a 3D-printed, 2-mm plastic tip. A gentle contact force of approximately 0.01 N was applied, ensuring minimal deformation of the lens surface. Pure tone stimuli were used across a frequency range of 1-30 kHz. For each frequency, 172 A-lines were collected (M-scan) while the OCT beam was maintained fixed at a location on the sample. The M scan was repeated at 96 transverse positions on the lens. The scan length varied inversely with frequency, ranging from 3 mm at 1-6 kHz to 1 mm at 20-30 kHz. As described previously [40, 42], displacement profiles over time (t) were extracted at each scan position and Fourier-transformed to convert the data into the frequency (f) domain. The phase and amplitude of the mechanical vibration were filtered using a lock-in bandwidth of ~ 250 Hz around the excitation frequency. Two-dimensional cross-sectional displacement images were generated by performing these steps for all scan positions. To calculate wave velocities, one-dimensional displacement profiles from the sample surface were obtained and Fourier-transformed to measure the wavenumber (k) of each wave. The phase velocity (v) was then calculated using the equation $v = 2\pi f/k$. A dispersion curve was constructed from the phase velocities corresponding to individual stimulus frequencies.

C. Bilayer guided wave model under tension

We modeled the lens using a tension-induced bilayer framework comprising a stiff top layer with thickness h and Young's modulus E_1 , and a semi-infinite soft substrate with Young's modulus E_2 . The stiff top layer represents the capsule while the soft substrate corresponds to the cortical tissue. The lens nucleus was excluded from the model, as its impact on wave dispersion was negligible at frequencies below 1 kHz. Both layers were assumed to be elastic, isotropic, and incompressible. The biaxial stresses in the top layer and substrate are denoted as σ_1 and σ_2 , respectively. Guided waves in this bilayer structure are subject to stress-free boundary conditions at the air-facing surface and continuity conditions at the interface between the layers. Using incremental dynamics theory [43, 44], the secular equation governing elastic guide wave propagation in the bilayer structure is derived (see Supplement 1):

$$\det(\mathbf{M}_{6 \times 6}) = 0, \quad (1)$$

where $\mathbf{M}_{6 \times 6}$ is a matrix with components given in Appendix. The relationship between wave angular frequency ω ($= 2\pi f$) and wavenumber k is determined by Eq. (1). The phase velocity v is then obtained as $v = \omega/\text{Re}(k)$.

D. Inverse method to extract mechanical parameters

Mechanical parameters were extracted from measured wave velocity dispersion curves using analytical solutions derived from bilayer model. In the stress-free state, the dispersion is described by $v = v(h, E_1, E_2; f)$, where f represents the stimulus frequency, and h , E_1 , and E_2 are input variables. The capsular thickness (h) was directly obtained from OCT images. The substrate modulus (E_2) was calculated using $E_2 = 3\rho v_{t2}^2$, where v_{t2} was estimated from wave velocities measured at low frequencies (1-2 kHz). The only remaining variable, E_1 (the capsule modulus), was determined by fitting the experimental dispersion curves in the stress-free state. Curve fitting was performed by minimizing the root-mean-square-error (RMSE) as the objective function, with the best fit found by identifying the minimum error. In the pre-stressed state, the dispersion is described by $v = v(h, E_1, E_2, \sigma_1, \sigma_2; f)$, where h , E_1 , and E_2 were determined from the stress-free state. The remaining variables, the stresses σ_1 and σ_2 , were extracted by fitting the dispersion curves measured in the pre-stressed state. As with the stress-free state, the best fit was identified by minimizing the RMSE.

E. Finite-element numerical modeling

Finite element analysis (FEA) was performed using Abaqus/CAE 6.14 (Dassault Systèmes, USA). An axisymmetric bilayer conoid-shape model was developed to simulate the lens capsule and cortex. The Young's moduli of the capsule and cortex were set to 1500 kPa and 30 kPa, respectively. To simulate tension from the zonular fibers, the lens model was subjected to a quasi-static stretch applied at multiple points on the side of the lens. Subsequently, a fixed-frequency excitation was applied to the top of the posterior capsule to model elastic wave propagation and dispersion. The model was discretized using approximately 110,000 axisymmetric solid elements (CAX8RH). Simulation convergence was carefully verified by comparing results with those obtained using a finer mesh and smaller time steps. The phase velocity was extracted from the spatiotemporal displacement field on the surface of the capsule. A Fourier transform was applied to determine the wavenumber (k) at each frequency (f). The phase velocity (v) was calculated using $v = 2\pi f/k$.

3. RESULTS

A. Wideband OCE measurements on isolated intact lenses

We performed OCE measurements on freshly isolated lenses from six-month-old pigs (Fig. 1). Figure 1B shows the experimental setup, where a contact PZT probe, vibrating at a given frequency, generates elastic waves, and the vertical displacement is detected by phase-sensitive OCT. For posterior lens measurements, the sample was flipped. The wave velocities measured along the lens surface across the frequency range of 1 to 30 kHz are plotted in Fig. 1C. The wave velocities exhibited a strong frequency dependency. While the viscoelastic properties of tissue contribute to frequency-dependent wave speeds, such pronounced dependency typically suggests a stiff surface overlying a softer interior, similar to tissues such as skin [41]. At low frequencies, where the wavelength far exceeds the thickness of the capsule, the capsule has minimal impact on wave velocity, which is mainly determined by the softer lens tissue. As the frequency increases, the wave's elastic energy becomes progressively concentrated within the stiffer capsule, resulting in higher velocities.

The velocity data revealed significant differences between the anterior and posterior lens surfaces. At low frequencies (1-2 kHz), phase velocities were only modestly different, indicating similar cortical stiffness on both sides. However, at higher frequencies (> 4 kHz), more pronounced differences emerged. OCT structural images (Fig. 1D) show that the anterior

capsule is thicker than the posterior capsule. Figure 1E presents OCE wave maps recorded at 2 kHz and 10 kHz, where wavelength decreases with increasing frequency on both surfaces. At 10 kHz, multiple wave cycles are observed. Previous, we have observed stronger attenuation of Rayleigh waves at 10 kHz in the cornea and skin [40-42], but here, the results indicate that the lens tissue exhibits a dominance of elasticity over viscosity.

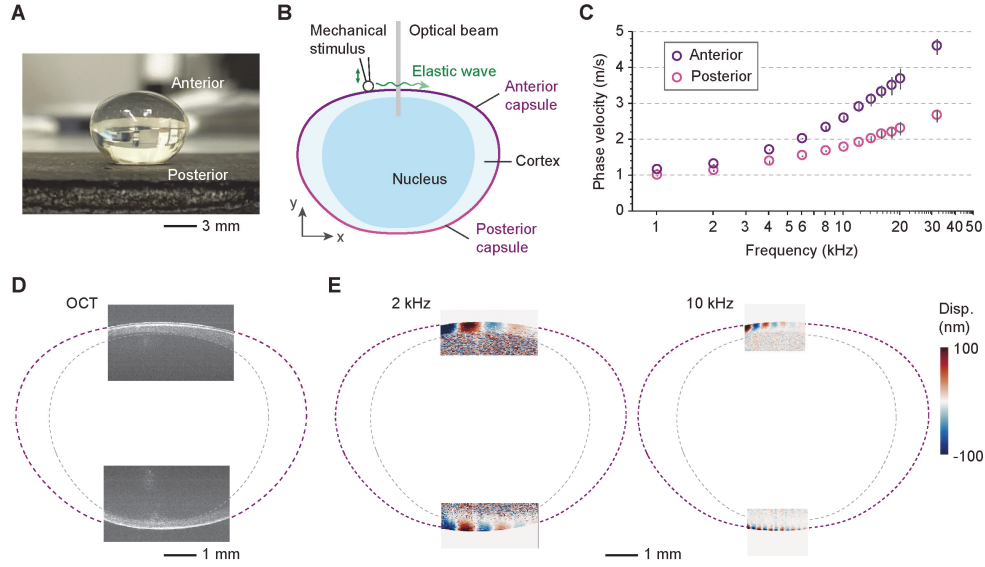


Fig. 1. OCE measurement on intact porcine lenses. (A) Photography of a 6-month-old porcine lens. (B) Schematic of the experimental setup. (C) Wave velocities measured on the anterior and posterior surfaces, presented as mean \pm S.D. ($n = 3$ measurements at different locations on one sample). (D) Cross-sectional OCT image of the lens. (E) OCE wave displacement profiles recorded at 2 kHz and 10 kHz. Dashed outlines denote the external surface, and dotted lines mark the interface between the cortex and nucleus.

B. A bilayer mechanical model under tension

To quantitatively interpret the data, we developed mechanical models for the lens. Figure 2A illustrates the lens model. The ILP is the highest at the nucleus center and decreases toward the lens periphery, varying as a function of the radial position r . For isolated lenses without external force, the capsular tension σ_1 arises from the internal pressure, $P(r)$; under force equilibrium [45],

$$\sigma_1 = \frac{P(R)R}{2h}, \quad (2)$$

where R is the radius of curvature of the lens surface, and h is the thickness of the capsule. The pressure gradient also induces deviatoric lateral stress in the lens tissue. By force balance (See Supplement 3),

$$\sigma_2(r) = \frac{r}{2} \frac{dP}{dr}. \quad (3)$$

To simplify this, we modeled the lens as a bilayer system under tension (Fig. 2B). The top layer represents the capsule, with Young's modulus E_1 , while the semi-infinite substrate represents the cortex, characterized by a uniform Young's modulus E_2 ($< E_1$) and uniform stress $\sigma_2 \approx \frac{R}{2} \frac{dP}{dr} \Big|_{r=R}$. The nucleus minimally contributes to wave dispersion for frequencies above 2 kHz.

When lenses are subjected to external forces, such as tension from zonular fibers, the capsular and cortical tensions are modified as follows:

$$\sigma_1 = \sigma_1^{ext} + \frac{P(R)R}{2h} \quad (4)$$

$$\sigma_2(r) = \sigma_2^{ext} + \frac{r}{2} \frac{dP}{dr}, \quad (5)$$

where σ_1^{ext} and σ_2^{ext} represent the tensions induced by the external force in the capsule and cortex, respectively.

For simplicity, we assumed elastic, isotropic, and incompressible materials. For each layer ($i=1, 2$), incremental parameters α_i , β_i and γ_i were derived from the fourth-order Eulerian elasticity tensor $\mathcal{A}^{(i)}$ as follows [44]: $\alpha_i = \mathcal{A}_{xyxy}^{(i)}$, $2\beta_i = \mathcal{A}_{xxxx}^{(i)} + \mathcal{A}_{yyyy}^{(i)} - 2\mathcal{A}_{xxyy}^{(i)} - 2\mathcal{A}_{xyyx}^{(i)}$, $\gamma_i = \mathcal{A}_{yxyx}^{(i)}$. Under small-strain biaxial stretching, the relationships are (see Supplement 1):

$$\alpha_i = \frac{1}{3}E_i + \frac{1}{3}\sigma_i, \beta_i = \frac{1}{3}E_i, \gamma_i = \frac{1}{3}E_i - \frac{2}{3}\sigma_i. \quad (6)$$

The bulk shear wave speed, v_{ti} , in an infinitely large layer is given by

$$\rho_i v_{ti}^2 = 0.333E_i + 0.333\sigma_i, \quad (7)$$

where ρ_i are the mass density. Guided waves in the tension-induced bilayer structure are governed by the secular equation (1). Figure 2C illustrate the solutions of the secular equation. At low frequency limit, the wave speed approaches a plateau at v_{R2} , and at high frequencies, it asymptotically reaches v_{R1} , where:

$$\rho_i v_{Ri}^2 = 0.304E_i + 0.392\sigma_i. \quad (8)$$

Note that v_{R1} and v_{R2} are similar to the bulk wave speeds given in Eq. (7) and exhibit slightly higher sensitivity to tension. The transition between these regimes begins at a critical frequency, f_{c2} , where the wave dispersion curve bifurcates into leaky surface-guided and bulk-wave-like branches. The critical frequency is given by

$$f_{c2} = C_1 \left(\frac{E_2}{E_1} \right) C_2 \frac{v_{t2}}{h}, \quad (9)$$

where $C_1 \approx 1990 \left(\frac{\sigma_1}{E_1} \right)^3 - 241 \left(\frac{\sigma_1}{E_1} \right)^2 + 7.2 \left(\frac{\sigma_1}{E_1} \right) + 0.16$ and $C_2 \approx 1 - 0.5 \exp(-90 \frac{\sigma_1}{E_1})$ (see Supplement 2). In the absence of tension ($\sigma_1 = 0$), f_{c2} simplifies to the result previously derived for tension-free bilayers [41]. Within the transition region, the guided wave velocity increases with frequency. The high-frequency plateau is reached at another critical frequency, $f_{c1} \approx v_{t1}/h$.

This formalism provides a powerful analytical tool for determining the key mechanical parameters σ_1 , σ_2 , E_1 , and E_2 from experimentally obtained wide-frequency velocity data. For typical accommodative porcine and human lenses, f_{c2} is expected to range between 100 Hz and 10 kHz, and f_{c1} would be close to 1 MHz. These frequencies fall within the capabilities of state-of-the-art OCE systems [39, 40]. However, accurately measuring wave velocities becomes increasingly difficult at higher frequencies, typically beyond 50 kHz, due to reduced wave

displacement. Notably, dispersion data over a substantial frequency range, such as 1-30 kHz, can still reveal sufficient features to determine the key parameters through curve fitting.

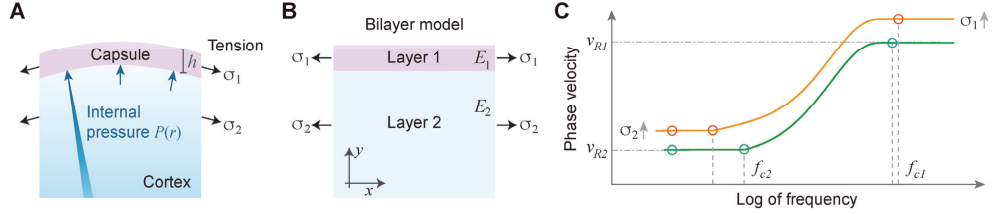


Fig. 2. The bilayer model under tension. **(A)** Schematic of the lens, illustrating the radial gradient of intra-lenticular pressure (blue arrows). **(B)** Equivalent bilayer model comprising a top layer (layer 1) and a semi-infinite substrate (layer 2). Young's moduli are denoted as E_1 and E_2 ($E_2 < E_1$). **(C)** Phase velocity of the guided wave as a function of frequency. The transition between low- and high-frequency regimes begins at the critical frequency f_{c2} , where the velocity increases from the Rayleigh wave velocity of the substrate v_{R2} to the Rayleigh wave velocity of the top layer v_{R1} . The high plateau of the phase velocity is reached at frequency f_{c1} . Increased tension raises the velocities and shifts the critical frequencies.

C. Quantification of intrinsic capsular tension

Six-month-old porcine lenses exhibited high elasticity during finger palpation. When a small incision was made on one side of the capsule, lens tissue visibly bulged through the opening (Fig. 3A). OCE measurements were performed on lenses before and after a complete circumferential incision of the capsule around the equator (Fig. 3B). After the incision, the posterior capsule exhibited noticeable shrinkage ($\sim 3\%$) as observed visually, whereas the anterior capsule showed less shrinkage. This indicates that the ILP-induced capsular tension in intact lenses is substantially greater in the posterior capsule than in the anterior capsule. Consistent with this observation, the anterior lens surface displayed smaller changes in wave profiles (Fig. 3C) and velocity dispersion (Fig. 3D). In contrast, the posterior surface showed significant changes in wave profiles (Fig. 3E) and velocities (Fig. 3F) following the release of capsular tension. Moreover, wave attenuation on the posterior surface increased markedly, showing a transition from predominantly elastic to viscoelastic behavior.

We applied the bilayer model to the OCE data and derived the following parameters. For the anterior capsule data in Fig. 3C, we estimated $h = 55 \mu\text{m}$, $E_1 = 2.5 \text{ MPa}$, $E_2 = 17 \text{ kPa}$. The ILP-induced anterior tensions were calculated to be $\sigma_1 = 20 \text{ kPa}$, and $\sigma_2 = 200 \text{ Pa}$. For the posterior capsule data in Fig. 3D, we obtained $h = 15 \mu\text{m}$, $E_1 = 1.2 \text{ MPa}$, and $E_2 = 7 \text{ kPa}$. The ILP-induced posterior tensions were measured to be $\sigma_1 = 41 \text{ kPa}$, and $\sigma_2 = 400 \text{ Pa}$. Parameters obtained from 6-month-old porcine lenses ($n = 5$ samples) were $E_1 = 1.89 \pm 0.82 \text{ MPa}$, $E_2 = 18 \pm 1 \text{ kPa}$, $\sigma_1 = 8 \pm 8 \text{ kPa}$, and $\sigma_2 = 150 \pm 30 \text{ Pa}$ for anterior capsules and cortices, and $E_1 = 1.32 \pm 0.32 \text{ MPa}$, and $E_2 = 7 \pm 2 \text{ kPa}$, $\sigma_1 = 44 \pm 4 \text{ kPa}$, and $\sigma_2 = 800 \pm 600 \text{ Pa}$ for posterior capsules and cortices.

Capsules were further isolated from the lenses (Fig. 3G) and placed loosely on a holder without external tension. OCE measurements demonstrated elastic waves propagation along the free-hanging anterior (Fig. 3H) and posterior capsules (Fig. 3I). Wave velocity dispersion curves were obtained (Fig. 3J) and fitted using a tension-free single-layer Lamb-wave model [46, 47]. The best-fit parameters obtained from three specimens from three different lenses were $E_1 = 1.25 \pm 0.15 \text{ MPa}$ for the anterior capsule and $E_1 = 1.05 \pm 0.12 \text{ MPa}$ for the posterior

capsule. These values match those previously derived from the intact lens using the bilayer model under tension, within the uncertainty of the fitting.

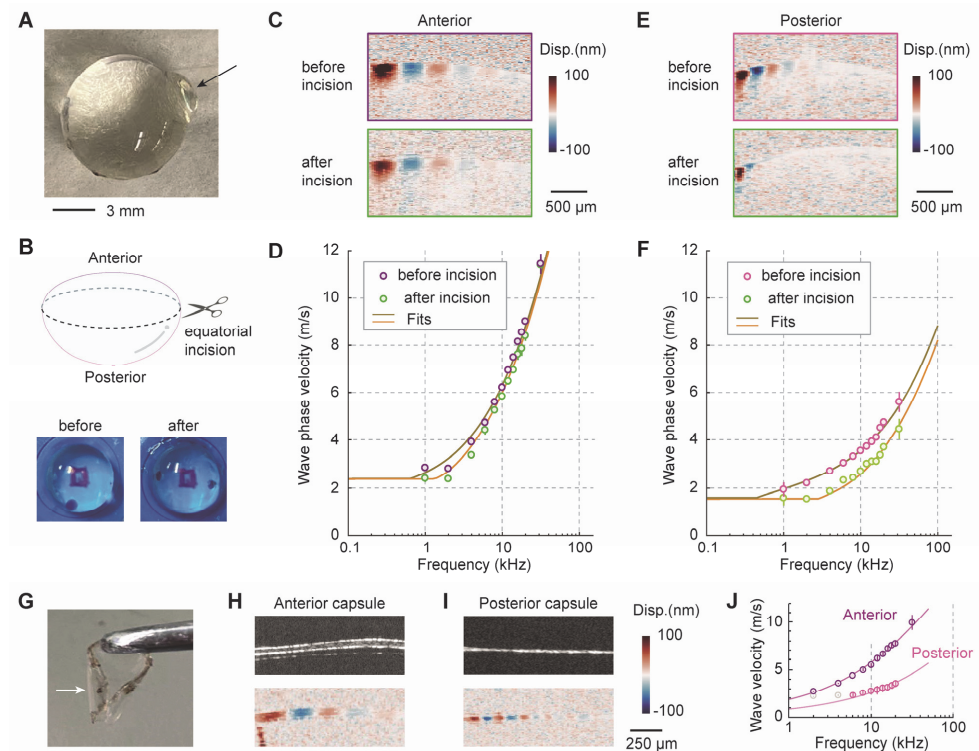


Fig. 3. The measurement of ILP-induced capsular tension. (A) Photograph showing lens tissue bulging through a small opening in the capsule. (B) Schematic representation of the circumferential incision of the lens capsule. (C) Wave profiles on the anterior lens before and after incision at 6 kHz. (D) Velocity dispersion curves for the anterior lens before and after incision. (E) Wave profiles on the posterior lens before and after incision at 6 kHz. (F) Velocity dispersion curves for the posterior lens before and after incision. (G) Photograph of an isolated anterior capsule. (H) Cross-sectional image (top) and wave profile at 12 kHz (bottom) of an isolated anterior capsule. (I) Cross-sectional image (top) and wave profile at 12 kHz (bottom) of an isolated posterior capsule. (J) Wave velocity dispersion curves for the isolated capsules. Error bars in (D), (F), and (J) represent standard deviation from 3 measurements at different locations of each sample.

D. A finite element model of the lens and zonular stretching

Finite element analysis (FEA) was performed using an axisymmetric lens model that included zonular ciliary fibers (Fig. 4A). The model parameters were $h = 48 \mu\text{m}$ (at zero stretch), $E_1 = 1.5 \text{ MPa}$, $E_2 = 30 \text{ kPa}$. Figure 4B shows the stress distribution in the lens under a radial stretch of 0.5 mm (5 mm in radius, $\sim 10\%$ stretch). The anterior capsule tension was approximately 70 kPa, while cortical lateral stress ranged from 700 Pa on the anterior side to 2 kPa at the equator. These results are consistent with previous reported values in the literature [48]. Figure 4B displays the displacement profile of elastic waves generated by a 10-kHz stimulus applied to the anterior capsule. The surface wave velocity was extracted by performing a Fourier transform of the displacement profile along the capsule. Figure 4C shows wave velocities (circles) measured under three different anterior capsular tension conditions: 0, 60, and 100 kPa, induced

by varying the ciliary stretch. The dispersion curves (solid lines) calculated using the bilayer model show excellent agreement with the FEA results. Slight deviations near low critical frequencies are attributed to the inhomogeneous stress distribution in the cortex in the FEA model, compared to the assumption of uniform stress in the bilayer model. Figure 4d presents a super-linear relationship between the anterior capsular tension versus applied stretch. Figure 4e plots the change in lens thickness versus applied stretch, showing lens thickness reduction with stretch [49]. Figure 4f plots the stretching force as a function of stretch distance [48-50].

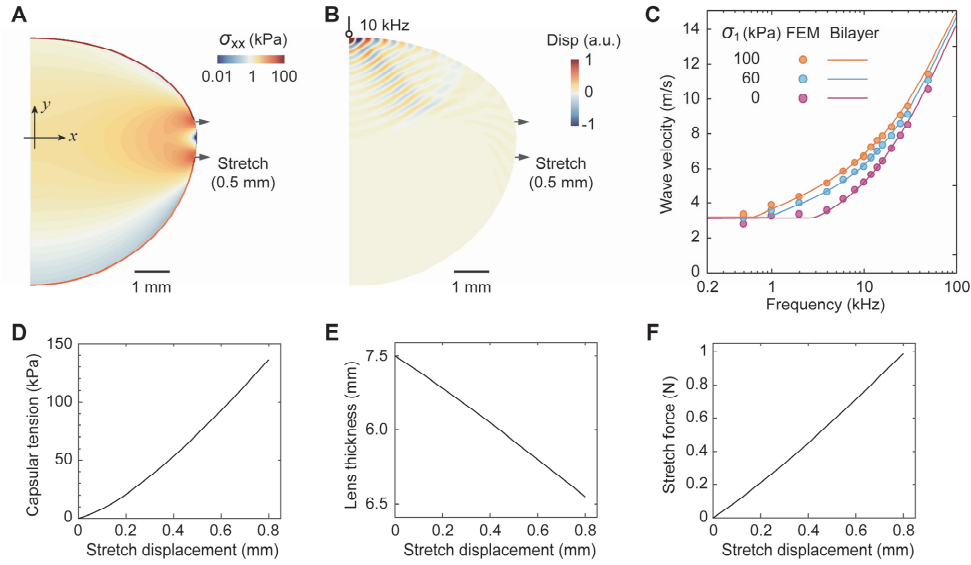


Fig. 4. Finite element lens model under zonular stretch. (A) Distribution of lateral stress (σ_{xx}) in the lens when the upper and lower equatorial points are stretched by a displacement of 0.5 mm. (B) Wave-field generated at an excitation frequency of 10 kHz. (C) Dispersion curves under different capsular tensions: 0, 60 kPa and 100 kPa, induced by a zonular stretch of 0, 0.45 mm, and 0.65 mm, respectively. Circles represent FEA results, while solid curves denote bilayer model results. Purple curve: $\sigma_1 = \sigma_2 = 0$, $h = 48 \mu\text{m}$. Blue curve: $\sigma_1 = 60 \text{ kPa}$, $\sigma_2 = 0.6 \text{ kPa}$, $h = 46 \mu\text{m}$. Orange curve: $\sigma_1 = 100 \text{ kPa}$, $\sigma_2 = 1 \text{ kPa}$, $h = 45 \mu\text{m}$. (D) Relationship between anterior capsular tension and applied stretch. (E) Relationship between lens thickness and applied stretch. (F) Relationship between force and applied stretch.

E. Quantification of capsular tension induced by biaxial stretching

To mimic the accommodation process, we stretched a lens *in situ* inside an eye globe using a biaxial stretcher (Fig. 5A). Figure 5B provides a schematic representation of the lens in both non-stretch (relaxed) and stretch conditions. The non-stretch condition corresponds to maximum accommodation, where zonular fiber forces are released, while the stretch condition simulates the lens under tension from zonule fiber forces [4, 32]. OCT images (Fig. 5C) reveal significant flattening of the anterior lens surface under axial stretch, estimated at approximately 4%. Upon stretching, the wavelength of elastic waves increased markedly (Fig. 5D). Figure 5E shows measured wave velocities in both relaxed and stretched conditions. Curve fitting of the dispersion data in the relaxed condition, using the bilayer model, yielded a Young's modulus (E_1) to be 1.79 MPa for the anterior capsule. Fitting of the stretched lens data indicated a capsular tension (σ_1) of 64 kPa and an effective cortical tension (σ_2) of 200 Pa.

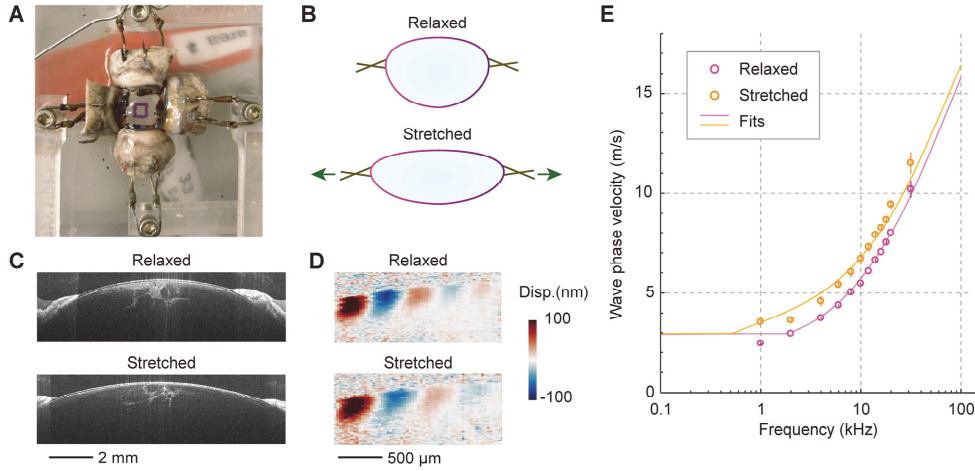


Fig. 5. Biaxial stretching of a porcine lens *in situ*. **(A)** Photograph of an eye globe mounted in a biaxial stretching device, applying tensional force to the surrounding sclera and ciliary zonular fibers. **(B)** Schematic representation of the lens in relaxed and stretched conditions. **(C)** OCT images showing the anterior lens in relaxed and stretch conditions. **(D)** OCE wave profiles at 6 kHz in relaxed and stretched conditions. **(E)** Wave velocities of the anterior lens in relaxed and stretched conditions. Circles represent the experimental mean values from three measurements at different locations on the sample, with error bars denoting standard deviation. Best-fit parameters were $h = 55 \mu\text{m}$, $E_1 = 1785 \text{ kPa}$, $E_2 = 26 \text{ kPa}$ for both conditions. Tensions were $\sigma_1 = \sigma_2 = 0 \text{ kPa}$ for the relaxed state and $\sigma_1 = 64 \text{ kPa}$, $\sigma_2 = 0.2 \text{ kPa}$ for the stretched state.

4. DISCUSSION AND CONCLUSION

Our results demonstrate the effectiveness of deriving mechanical parameters from leaky surface waves, which are supported in structures with a stiff surface and softer interior. These highly dispersive waves exist between two critical frequencies, f_{c2} and f_{c1} . The dispersion curves in this frequency range exhibit rich features from which elastic moduli and tensions within the structure can be derived. Utilizing a recently developed high-frequency wideband OCE system, we successfully applied this principle to the lens capsule-tissue system, determining both intrinsic and externally induced tensions in the lens capsule with kPa-scale resolution. To the best of our knowledge, this represents the first *in situ* measurement of capsular tension within an eyeball.

For lens parameters ($E_1 = 1.5 \text{ MPa}$, $E_2 = 10 \text{ kHz}$, $h = 55 \mu\text{m}$, $\rho_i = 1050 \text{ kg/m}^3$ and σ_1 ranging from 0 to 60 kPa), we estimate f_{c2} to be 600-800 Hz and f_{c1} to be 400 kHz. Conventional OCE systems, limited to a frequency range of 2-4 kHz, were insufficient for lens capsule measurements. In this study, optimized mechanical stimulation and system noise control enabled us to reliably obtain wave velocities up to 30 kHz. This wideband capability was critical for tension measurement. The upper frequency limit in our system is constrained by the signal-to-noise ratio (SNR), as wave displacement decreases and attenuation increases with frequency. Further extending the high frequency limit could improve the accuracy and precision of curve fit parameters.

Normal ILP in human eyes are considered to be similar to intraocular pressure (IOP), ranging from 10 to 20 mmHg (1.3 to 2.6 kPa). In a detailed study of murine lenses, an intracellular microelectrode sensor revealed a parabolic ILP profile, decreasing from $\sim 330 \text{ mmHg}$ (44 kPa) at the center to near zero at the surface [51]. This gradient pressure drives intracellular fluid circulation within the lens through gap junction channels [51]. Using isolated lenses from six-month-old pigs (N=6) free from external tension, we measured a posterior

capsular tension (σ_1) of 44 kPa and a cortical tension (σ_2) of 800 Pa. Applying the Young-Laplace relation ($\sigma_1 = PR/2h$ with $h = 15 \mu\text{m}$ and $R = 6 \text{ mm}$), we calculated the hydrostatic ILP at the posterior surface to be 22 Pa. From $\sigma_2 = R/2 (dP/dr)$, a pressure gradient of 260 Pa/mm was estimated at the posterior surface.

We measured the Young's moduli of the anterior and posterior porcine capsules to be $1.89 \pm 0.8 \text{ MPa}$ and $1.32 \pm 0.3 \text{ MPa}$, respectively. These values are consistent with reported ranges in the literature: 1.5 to 6 MPa from spinning tests [16], 0.3 – 6 MPa from tensile tests [6, 34, 52, 53]. Capsulorhexis, a procedure involving the removal of part of the anterior lens capsule, is a standard technique in cataract surgery [5]. Understanding the stiffness and tension of the anterior capsule prior to surgery could assist physicians in optimizing short-term surgery outcome. Additionally, the ability to measure capsular tension after the placement of intraocular implants could prove valuable for improving long-term surgical success.

This study has several limitations. First, our current model assumes that the lens capsule and cortex are elastic and isotropic. However, previous studies have demonstrated the viscoelastic nature of the lens and its influence on wave velocity [30, 54]. Future work should incorporate a more advanced model that accounts for viscoelasticity and anisotropy in these layers [55]. Second, the current stretching device applies forces to the sclera rather than directly to the zonule fibers. The device could be refined to better mimic the accommodative process [50]. Finally, the current OCE system relies on contact mechanical stimulation. Several studies have shown that acoustic radiation forces from focused ultrasound can generate elastic waves with substantial displacement amplitudes in the lens. Integrating non-contact ultrasound stimulation into wideband OCE could enable clinical translation of this method for evaluating the human lens.

In our biaxial lens stretching experiment, the OCE method effectively detected changes in anterior capsular tension, ranging from near zero in the fully relaxed state to 64 kPa under a stretched condition (4% strain). This result highlights the promising translational potential of acousto-optical OCE for a range of clinical applications, including the diagnosis and monitoring of accommodative dysfunctions such as presbyopia, as well as the optimization of capsulectomy procedures.

Beyond ophthalmic applications, this acousto-optical elastography method could also be valuable for measuring stress, strain, and mechanical properties in various tissues and biomaterials. Potential applications include assessing tension in blood vessels, tendons, ligaments, and skin.

Funding. National Institutes of Health (R01-EY033356, R01-EY034857).

Acknowledgements.

Disclosures. The authors declare no conflicts of interest.

Data availability. Data underlying the results presented in this paper are not publicly available at this time but may be obtained from the authors upon reasonable request.

Appendix

The components of the matrix $\mathbf{M}_{6 \times 6}$ are as follows:

$$\begin{aligned} M_{11} &= s_1, M_{12} = s_2, M_{13} = -s_1, M_{14} = -s_2, M_{15} = -s_1^*, M_{16} = -s_2^*, \\ M_{21} &= 1, M_{22} = 1, M_{23} = 1, M_{24} = 1, M_{25} = -1, M_{26} = -1, \end{aligned} \quad (\text{A1})$$

$$\begin{aligned}
M_{31} &= \gamma_1(1 + s_1^2), M_{32} = \gamma_1(1 + s_2^2), M_{33} = \gamma_1(1 + s_1^2), M_{34} = \\
&\gamma_1(1 + s_2^2), M_{35} = -\gamma_2(1 + s_1^{*2}), M_{36} = -\gamma_2(1 + s_2^{*2}), \\
M_{41} &= \gamma_1 s_1(1 + s_2^2), M_{42} = \gamma_1 s_2(1 + s_1^2), M_{43} = -\gamma_1 s_1(1 + s_2^2), \\
M_{44} &= -\gamma_1 s_2(1 + s_1^2), M_{45} = -\gamma_2 s_1^*(1 + s_2^{*2}), M_{46} = -\gamma_2 s_2^*(1 + s_1^{*2}), \\
M_{51} &= (1 + s_1^2)\exp(s_1 kh), M_{52} = (1 + s_2^2)\exp(s_2 kh), M_{53} = \\
&(1 + s_1^2)\exp(-s_1 kh), M_{54} = (1 + s_2^2)\exp(-s_2 kh), M_{55} = 0, M_{56} = 0, \\
M_{61} &= s_1(1 + s_2^2)\exp(s_1 kh), M_{62} = s_2(1 + s_1^2)\exp(s_2 kh), \\
M_{63} &= -s_1(1 + s_2^2)\exp(-s_1 kh), M_{64} = -s_2(1 + s_1^2)\exp(-s_2 kh), \\
M_{65} &= 0, M_{66} = 0.
\end{aligned}$$

Here, $\gamma_1 = (E_1 - 2\sigma_1)/3$, $\gamma_2 = (E_2 - 2\sigma_2)/3$. s_1 and s_2 are roots of the quartic equation:

$$\gamma_1 s^4 - \left(\frac{2}{3}E_1 - \rho_1 \frac{\omega^2}{k^2}\right) s^2 + \frac{E_1 + \sigma_1}{3} - \rho_1 \frac{\omega^2}{k^2} = 0. \quad (\text{A2})$$

s_1^* and s_2^* are roots of the quartic equation:

$$\gamma_2 s^{*4} - \left(\frac{2}{3}E_2 - \rho_2 \frac{\omega^2}{k^2}\right) s^{*2} + \frac{E_2 + \sigma_2}{3} - \rho_2 \frac{\omega^2}{k^2} = 0. \quad (\text{A3})$$

ρ_1 and ρ_2 denote the densities of the top layer and substrate, respectively. $\omega (= 2\pi f)$ is the angular frequency, and k is the wavenumber.

Supplemental document. See Supplement 1-3 for supporting content.

REFERENCES

1. D. J. Coleman, "Unified model for accommodative mechanism," *Am. J. Ophthalmol.* **69**, 1063-1079 (1970).
2. E. Fincham, "The coincidence optometer," *Proc. Phys. Soc.* **49**, 456 (1937).
3. R. A. Schachar, "Cause and treatment of presbyopia with a method for increasing the amplitude of accommodation," *Ann. Ophthalmol.* **24**, 445-447, 452 (1992).
4. H. v. Helmholtz, "Ueber die accommodation des auges," *Archiv für Ophthalmologie* **1**, 1-74 (1855).
5. S. Krag and T. T. Andreassen, "Mechanical properties of the human lens capsule," *Prog. Retin. Eye Res.* **22**, 749-767 (2003).
6. S. Krag and T. T. Andreassen, "Mechanical properties of the human posterior lens capsule," *Investig. Ophthalmol. Vis. Sci.* **44**, 691-696 (2003).
7. M. He, A. Abdou, K. S. Naidoo, *et al.*, "Prevalence and correction of near vision impairment at seven sites in China, India, Nepal, Niger, South Africa, and the United States," *Am. J. Ophthalmol.* **154**, 107-116. e101 (2012).
8. B. A. Holden, T. R. Fricke, S. M. Ho, *et al.*, "Global vision impairment due to uncorrected presbyopia," *Arch. Ophthalmol.* **126**, 1731-1739 (2008).
9. R. Fisher and B. Pettet, "The postnatal growth of the capsule of the human crystalline lens," *J. Anat.* **112**, 207 (1972).
10. N. M. Ziebarth, D. Borja, E. Arrieta, *et al.*, "Role of the lens capsule on the mechanical accommodative response in a lens stretcher," *Investig. Ophthalmol. Vis. Sci.* **49**, 4490-4496 (2008).

11. E. A. Hermans, P. J. Pouwels, M. Dubbelman, *et al.*, "Constant volume of the human lens and decrease in surface area of the capsular bag during accommodation: an MRI and Scheimpflug study," *Investig. Ophthalmol. Vis. Sci.* **50**, 281-289 (2009).
12. S. A. Strenk, J. L. Semmlow, L. M. Strenk, *et al.*, "Age-related changes in human ciliary muscle and lens: a magnetic resonance imaging study," *Investig. Ophthalmol. Vis. Sci.* **40**, 1162-1169 (1999).
13. A. Glasser, "Restoration of accommodation: surgical options for correction of presbyopia," *Clin. Exp. Optom.* **91**, 279-295 (2008).
14. K. Wang and B. K. Pierscionek, "Biomechanics of the human lens and accommodative system: Functional relevance to physiological states," *Prog. Retin. Eye Res.* **71**, 114-131 (2019).
15. H. Burd, G. Wilde, and S. Judge, "An improved spinning lens test to determine the stiffness of the human lens," *Exp. Eye Res.* **92**, 28-39 (2011).
16. R. Fisher, "The elastic constants of the human lens," *J. Physiol.* **212**, 147-180 (1971).
17. G. Wilde, H. Burd, and S. Judge, "Shear modulus data for the human lens determined from a spinning lens test," *Exp. Eye Res.* **97**, 36-48 (2012).
18. K. R. Heys, S. L. Cram, and R. J. Truscott, "Massive increase in the stiffness of the human lens nucleus with age: the basis for presbyopia?," (2004).
19. H. A. Weeber, G. Eckert, W. Pechhold, *et al.*, "Stiffness gradient in the crystalline lens," *Graefes Arch. Clin. Exp. Ophthalmol.* **245**, 1357-1366 (2007).
20. H. A. Weeber, G. Eckert, F. Soergel, *et al.*, "Dynamic mechanical properties of human lenses," *Exp. Eye Res.* **80**, 425-434 (2005).
21. A. Glasser and M. C. Campbell, "Biometric, optical and physical changes in the isolated human crystalline lens with age in relation to presbyopia," *Vision Res.* **39**, 1991-2015 (1999).
22. K. W. Hollman, M. O'Donnell, and T. N. Erpelding, "Mapping elasticity in human lenses using bubble-based acoustic radiation force," *Exp. Eye Res.* **85**, 890-893 (2007).
23. S. Yoon, S. Aglyamov, A. Karpouk, *et al.*, "A high pulse repetition frequency ultrasound system for the ex vivo measurement of mechanical properties of crystalline lenses with laser-induced microbubbles interrogated by acoustic radiation force," *Phys. Med. Biol.* **57**, 4871 (2012).
24. Y. S. Ambekar, M. Singh, J. Zhang, *et al.*, "Multimodal quantitative optical elastography of the crystalline lens with optical coherence elastography and Brillouin microscopy," *Biomed. Opt. Express* **11**, 2041-2051 (2020).
25. N. M. Ziebarth, E. Arrieta, W. J. Feuer, *et al.*, "Primate lens capsule elasticity assessed using Atomic Force Microscopy," *Exp. Eye Res.* **92**, 490-494 (2011).
26. S. Besner, G. Scarcelli, R. Pineda, *et al.*, "In vivo Brillouin analysis of the aging crystalline lens," *Investig. Ophthalmol. Vis. Sci.* **57**, 5093-5100 (2016).
27. G. Scarcelli, P. Kim, and S. H. Yun, "In vivo measurement of age-related stiffening in the crystalline lens by Brillouin optical microscopy," *Biophys. J.* **101**, 1539-1545 (2011).
28. Y. Chen, S. Ye, Q. Wang, *et al.*, "In situ assessment of lens elasticity with noncontact optical coherence elastography," *Biomed. Opt. Express* **13**, 6671-6681 (2022).
29. Y. Li, J. Zhu, J. J. Chen, *et al.*, "Simultaneously imaging and quantifying in vivo mechanical properties of crystalline lens and cornea using optical coherence elastography with acoustic radiation force excitation," *APL Photonics* **4**, 106104 (2019).

30. T. Mekonnen, C. Zevallos-Delgado, H. Zhang, *et al.*, "The lens capsule significantly affects the viscoelastic properties of the lens as quantified by optical coherence elastography," *Front. Bioeng. Biotechnol.* **11**, 1134086 (2023).
31. R. Li, X. Qian, C. Gong, *et al.*, "Simultaneous Assessment of the Whole Eye Biomechanics Using Ultrasonic Elastography," *IEEE Trans. Biomed. Eng.* (2022).
32. R. Fisher, "The significance of the shape of the lens and capsular energy changes in accommodation," *J. Physiol.* **201**, 21-47 (1969).
33. J. E. Morgan, R. B. Ellingham, R. D. Young, *et al.*, "The mechanical properties of the human lens capsule following capsulorhexis or radiofrequency diathermy capsulotomy," *Arch. Ophthalmol.* **114**, 1110-1115 (1996).
34. S. Krag and T. T. Andreassen, "Biomechanical measurements of the porcine lens capsule," *Exp. Eye Res.* **62**, 253-260 (1996).
35. S. Krag, T. Olsen, and T. T. Andreassen, "Biomechanical characteristics of the human anterior lens capsule in relation to age," *Investig. Ophthalmol. Vis. Sci.* **38**, 357-363 (1997).
36. L. Werner, "Glistenings and surface light scattering in intraocular lenses," *J. Cataract Refract. Surg.* **36**, 1398-1420 (2010).
37. C. Simsek, S. Oto, G. Yilmaz, *et al.*, "Comparison of the mechanical properties of the anterior lens capsule in senile cataract, senile cataract with trypan blue application, and pseudoexfoliation syndrome," *J. Cataract Refract. Surg.* **43**, 1054-1061 (2017).
38. V. M. Sueiras, V. T. Moy, and N. M. Ziebarth, "Lens capsule structure assessed with atomic force microscopy," *Mol. Vis.* **21**, 316 (2015).
39. X. Feng, G.-Y. Li, and S.-H. Yun, "Ultra-wideband optical coherence elastography from acoustic to ultrasonic frequencies," *Nat. Commun.* **14**, 4949 (2023).
40. G.-Y. Li, X. Feng, and S.-H. Yun, "In vivo Optical Coherence Elastography Unveils Spatial Variation of Human Corneal Stiffness," *IEEE Trans. Biomed. Eng.* (2023).
41. X. Feng, G.-Y. Li, A. Ramier, *et al.*, "In vivo stiffness measurement of epidermis, dermis, and hypodermis using broadband Rayleigh-wave optical coherence elastography," *Acta Biomater.* **146**, 295-305 (2022).
42. G.-Y. Li, X. Feng, and S.-H. Yun, "Simultaneous tensile and shear measurement of the human cornea in vivo using S0-and A0-wave optical coherence elastography," *Acta Biomater.* **175**, 114-122 (2024).
43. N. Nam, J. Merodio, R. Ogden, *et al.*, "The effect of initial stress on the propagation of surface waves in a layered half-space," *Int. J. Solids Struct.* **88**, 88-100 (2016).
44. R. W. Ogden, "Incremental statics and dynamics of pre-stressed elastic materials," in *Waves in nonlinear pre-stressed materials* (Springer, 2007), pp. 1-26.
45. J. Pellicer, V. Garcia-Morales, and M. Hernandez, "On the demonstration of the Young-Laplace equation in introductory physics courses," *Phys. Educ.* **35**, 126 (2000).
46. Z. Han, J. Li, M. Singh, *et al.*, "Optical coherence elastography assessment of corneal viscoelasticity with a modified Rayleigh-Lamb wave model," *J. Mech. Behav. Biomed. Mater.* **66**, 87-94 (2017).
47. A. Ramier, A. M. Eltony, Y. Chen, *et al.*, "In vivo measurement of shear modulus of the human cornea using optical coherence elastography," *Sci Rep* **10**, 17366 (2020).
48. E. Lanchares, R. Navarro, and B. Calvo, "Hyperelastic modelling of the crystalline lens: Accommodation and presbyopia," *J. Optom.* **5**, 110-120 (2012).
49. H. M. Pour, S. Kanapathipillai, K. Zarrabi, *et al.*, "Stretch - dependent changes in surface profiles of the human crystalline lens during accommodation: A finite element study," *Clin. Exp. Optom.* **98**, 126-137 (2015).

50. F. Manns, J.-M. Parel, D. Denham, *et al.*, "Optomechanical response of human and monkey lenses in a lens stretcher," *Investig. Ophthalmol. Vis. Sci.* **48**, 3260-3268 (2007).
51. J. Gao, X. Sun, L. C. Moore, *et al.*, "Lens intracellular hydrostatic pressure is generated by the circulation of sodium and modulated by gap junction coupling," *J. Gen. Physiol.* **137**, 507-520 (2011).
52. C. C. Danielsen, "Tensile mechanical and creep properties of Descemet's membrane and lens capsule," *Exp. Eye Res.* **79**, 343-350 (2004).
53. W. O'Neill and J. Doyle, "A thin shell deformation analysis of the human lens," *Vision Res.* **8**, 193-206 (1968).
54. H. Zhang, M. Singh, F. Zvietcovich, *et al.*, "Age-related changes in the viscoelasticity of rabbit lens characterised by surface wave dispersion analysis," *Quantum Electron.* **52**, 42 (2022).
55. Y. Jiang, S. Ma, and Y. Cao, "Guided wave elastography of jugular veins: Theory, method and in vivo experiment," *J. Biomech.* **160**, 111828 (2023).